

LPCVD Grown Si-Doped β -Ga₂O₃ Films with Promising Electron Mobilities

Saleh Ahmed Khan¹, Ahmed Ibreljic¹, Stephen Margiotta¹, A F M Anhar Uddin Bhuiyan^{1, a)}

¹Department of Electrical and Computer Engineering, University of Massachusetts Lowell, MA 01854, USA

^{a)} Corresponding author Email: anhar_bhuiyan@uml.edu

Abstract

In this work, we systematically investigated the growth of Si-doped β -Ga₂O₃ films using Low pressure chemical vapor deposition (LPCVD) system, achieving high room temperature (RT) hall mobilities of 162 cm²/V·s and 149 cm²/V·s at carrier concentrations of 1.51×10^{17} cm⁻³ and 1.15×10^{17} cm⁻³, respectively for homoepitaxial (010) β -Ga₂O₃ film grown on β -Ga₂O₃ substrates and heteroepitaxial ($\bar{2}01$) β -Ga₂O₃ film grown on off-axis c-sapphire substrate with 6° miscut- representing the highest mobilities reported for LPCVD-grown β -Ga₂O₃ materials. Carrier concentrations were precisely tuned by varying SiCl₄ flow rates at growth temperature of 1000 °C, resulting in concentrations ranging from 1.15×10^{17} to 1.19×10^{19} cm⁻³ as confirmed by both Hall and capacitance-voltage (C-V) measurements. The films exhibited high crystalline quality, confirmed by high resolution X-ray diffraction (XRD) and Raman spectroscopy, indicating phase purity and structural integrity. Surface morphologies characterized by field-emission scanning electron microscope (FESEM) and atomic force microscopy (AFM) showed a strong correlation between carrier concentrations and surface smoothness, with lower concentration resulting in reduced RMS roughness. Secondary Ion Mass Spectrometry (SIMS) analysis revealed uniform Si incorporation, with low carbon, hydrogen, and chlorine impurities below detection limits, indicating high purity of the films. A high low-temperature peak mobility exceeding >843 cm²/V·s was achieved for ($\bar{2}01$) β -Ga₂O₃ heteroepitaxial films at 80 K, highlighting the high purity and low compensation of these films. These findings emphasize the potential of LPCVD growth system for

producing high-purity β -Ga₂O₃ films with thickness ranging between ~2.3-11.7 μm and faster growth rates (~4.7-17 $\mu\text{m/hr}$), promising transport properties, controllable doping, and scalability for developing high power vertical devices.

Keywords: *Ultra-wide bandgap semiconductor, Low pressure Chemical Vapor Deposition LPCVD, β -Ga₂O₃, electron mobilities, Si doping*

As the demand for advanced power-switching devices intensifies with the global shift toward electrification, semiconductor materials capable of operating under high voltage are becoming increasingly vital. While wide-bandgap materials such as SiC and GaN have surpassed Si for high-power applications, ultra-wide bandgap materials, particularly β -Ga₂O₃ are now gaining prominence as leading candidates for the next generation of high-performance power electronics due to its ultra-wide bandgap energy (~4.8 eV), placing it in the deep ultraviolet spectrum. The controllable n-type doping and high breakdown field strength of β -Ga₂O₃, projected to reach up to 8 MV/cm, surpasses that of SiC and GaN, making it a prime candidate for high voltage switching applications [1]. Moreover, β -Ga₂O₃ is unique in its ability to be grown by melt-based growth methods [2], offering scalability and cost-effectiveness through larger substrate sizes, enabling significant advancements in developing high power devices. In recent years, significant progress in β -Ga₂O₃-based power diodes and transistors have achieved multi-KV breakdown voltages, making them well-suited for applications such as electric vehicles, power grid, renewable energy, and defense. Vertical device architectures, in particular, are highly desirable for high-power applications as they allow for superior current drive and efficient field termination [3-18]. Achieving thick drift layers with low background carrier concentration is crucial for the scalability and performance of these devices. While several epitaxial growth techniques have been employed to grow β -Ga₂O₃ films, such as hydride vapor phase epitaxy (HVPE) [19-21], metalorganic

chemical vapor deposition (MOCVD) [22-33], LPCVD [34-40], and molecular beam epitaxy (MBE) [41-48], each has its own limitations. HVPE, for instance, is known for its rapid growth rates ($\sim 10\text{-}250\ \mu\text{m/h}$), making it a dominant choice for vertical device demonstrations. However, HVPE's fast growth rates often result in surface roughness that requires chemical-mechanical polishing before device fabrication. Recent advances in MBE growth technique [44-48], particularly suboxide and hybrid plasma-assisted MBE, has demonstrated controllable Si doping of $\beta\text{-Ga}_2\text{O}_3$ with promising mobilities [44,46] and higher growth rates ($\sim 1\ \mu\text{m/hr}$) [45]. Among these techniques, MOCVD is considered as a highly promising method for growing $\beta\text{-Ga}_2\text{O}_3$ films due to its ability to produce superior crystalline quality and controlled doping. MOCVD growth using triethylgallium (TEGa) and trimethylgallium (TMGa) has demonstrated record-high electron mobilities with low doping concentrations [22-24, 30]. However, MOCVD faces challenges in achieving higher growth rates, especially with TEGa, while TMGa allows for higher growth rates but introduces issues such as surface defects and high carbon incorporation, degrading material purity, surface quality, and transport properties [24]. In contrast, LPCVD offers several advantages for the growth of $\beta\text{-Ga}_2\text{O}_3$ films. LPCVD provides precise control over doping concentrations, minimizes impurity incorporation, and enables smoother, more uniform surfaces with much higher growth rates ($>10\ \mu\text{m/h}$) [34-40]. This is particularly advantageous for high-power applications, where thicker drift layer, surface quality, background impurities and doping precision are critical. Unlike MOCVD, which relies on metal-organic precursors susceptible to introducing unwanted impurities, LPCVD uses metallic Ga as a precursor, potentially enabling higher material purity and improved electron mobility. The controlled low-pressure environment also facilitates the deposition of thick drift layers with minimal defects [39]. LPCVD eliminates the use of organic ligands, preventing the risk of carbon contamination and enabling a faster decomposition process,

resulting in higher growth rates, improved lattice stability with less defects, while the low-pressure environment ensures uniform film growth by improving precursor adsorption and minimizing diffusion barriers. Numerical simulation studies, such as those using computational fluid dynamics [34], have been explored to analyze gas-phase reactions and mass transport limitations in LPCVD growth systems. Additionally, advanced simulation techniques such as density functional theory (DFT) and mesoscopic phase-field modeling [49, 50] provide a theoretical framework that could complement experimental efforts by offering insights into factors such as gas-phase dynamics, temperature gradients, and defect formation during LPCVD growth. Previous experimental studies on LPCVD-grown β -Ga₂O₃ have shown great potential in achieving high quality films [34-40]. In this current study, we seek to further explore LPCVD systems to push the current boundaries of electrical transport and structural quality of both homo- and hetero-epitaxial β -Ga₂O₃ films with a goal of achieving superior electron mobility while maintaining decent surface morphologies with faster growth rates. By fine-tuning LPCVD process parameters- such as temperature, gas flow rates, and source-substrate distances, high-quality films with promising electron mobilities and controllable doping was achieved, highlighting the potential of LPCVD system for the scalable production of thick β -Ga₂O₃ films for developing high power vertical devices.

The β -Ga₂O₃ growths have been performed in a custom built LPCVD system on off-axis c-sapphire substrates with 6° offcut and (010) β -Ga₂O₃ Fe-doped substrates. All the samples were cleaned using acetone, IPA and DI water followed by N₂ drying. Argon (99.9999% purity) has been utilized as the neutral carrier and purge gas; oxygen (99.999% purity) and gallium pellets (99.99999% purity) were used as O- and Ga- source precursors, respectively. SiCl₄ (flow rates: 0.03 to 0.5 sccm) has been used as the n-type dopant source. The growths were performed with Ar and O₂ flows of 200 and 20 sccm, respectively. The growth temperature was 1000°C and the

growth pressure was ~ 1.5 Torr. Ga source-to-substrate distances were tuned between 1.5 and 3.5 cm. The surface morphologies were characterized using a JEOL JSM 7401F FESEM and a Park XE-100 AFM systems. The thickness of homoepitaxial films were estimated from SIMS and FESEM cross-sectional images of the coloaded films grown on c-plane sapphire. The crystalline structure and quality were evaluated using XRD, performed with a Rigaku SmartLab tool equipped with a Cu $K\alpha$ radiation source ($\lambda=1.5418$ Å). The Raman spectroscopy has been carried out utilizing a Horiba LabRam Evolution Multiline Raman Spectrometer ($\lambda = 532$ nm). Transport properties were measured using van der Pauw-Hall configuration using the Ecopia HMS-5300 Hall effect measurement system from room to low temperatures (80 K). In order to measure transport properties by Hall measurements, 30/100 nm Ti/Au ohmic contacts were deposited on the four corners of each homoepitaxial β -Ga₂O₃ film. Vertical Schottky barrier diode structures using LPCVD homoepitaxial films grown on Sn-doped (010) β -Ga₂O₃ substrates were fabricated for C-V measurements. Device fabrication began with the deposition of a Ti/Au (30/100 nm) Ohmic metal stack on the backside of the substrates via E-beam evaporation, followed by rapid thermal in a nitrogen atmosphere at 470°C for 1 minute. Subsequently, Schottky C-V pads were lithographically defined, and a Schottky metal stack of Ni/Au (20/100 nm) was deposited on top of β -Ga₂O₃ layer. The C-V measurements were conducted using a Keithly 4200A parameter analyzer.

The FESEM images of the surface morphologies of LPCVD-grown β -Ga₂O₃ films on (010) β -Ga₂O₃ native substrates and off-axis c-sapphire substrates with a 6° offcut are shown in Figure 1. Figures 1(a-c) show the homoepitaxial films grown with different carrier concentrations, ranging from 1.51×10^{17} to 1.19×10^{19} . All samples exhibit a diagonal terrace-like morphology with multiple steps, consistent with previous reports on LPCVD-grown β -Ga₂O₃ films [35-37]. A

strong relationship between surface morphology and carrier concentrations can be observed: as the dopant incorporation decrease, the surface becomes smoother, with smaller features, which is also accompanied by an increase in electron mobility. Figures 1(d-f) show heteroepitaxial $(\bar{2}01)$ β - Ga_2O_3 film surfaces grown on 6° offcut c-plane sapphire, where step-flow growth along the offcut is evident. A similar trend is observed- higher doping concentrations lead to rougher surface morphology. To further investigate the surface roughness, AFM imaging was performed. Figures 2(a) and (b) show AFM scans ($5 \times 5 \mu\text{m}^2$) of homoepitaxial β - Ga_2O_3 films with doping concentrations of $1.51 \times 10^{17} \text{ cm}^{-3}$ and $1.39 \times 10^{18} \text{ cm}^{-3}$, yielding RMS roughness values of 2.65 nm (film thickness: $3.40 \mu\text{m}$) and 3.26 nm (film thickness: $3.37 \mu\text{m}$), respectively, comparable to previously reported LPCVD-grown films [35-37]. Figure 2(c) and (d) presents the AFM scans of heteroepitaxial β - Ga_2O_3 film surfaces with doping concentrations of $2.27 \times 10^{17} \text{ cm}^{-3}$ and $1.46 \times 10^{18} \text{ cm}^{-3}$, revealing clear and distinguishable steps along the offcut and an RMS roughness of ranging between 4.29 and 5.14 nm, measured over a $2 \times 2 \mu\text{m}^2$ area.

To investigate the crystalline structure and quality of the films, XRD ω - 2θ and ω -rocking curve scans were performed, as shown in Figures 3(a) and (b) for β - Ga_2O_3 homoepitaxial and heteroepitaxial films, respectively, with varying doping concentrations. The wide-range ω - 2θ scan in the inset of Figure 3(a) reveals a distinct, high-intensity (020) β - Ga_2O_3 peak for the homoepitaxial film, while both $(\bar{4}02)$ and $(\bar{8}04)$ peaks from $(\bar{2}01)$ β - Ga_2O_3 films are observed in the inset of Figure 3(b) for the heteroepitaxial growth on c-sapphire with a 6° miscut. No additional peaks associated with other planes and phases of Ga_2O_3 (α , γ , δ , ϵ) were detected, indicating the successful growth of single-crystal β - Ga_2O_3 films. Lower rocking curve FWHM values of 67, 63, and 124 arc-sec were observed for the homoepitaxial films with doping concentrations of 1.51×10^{17} , 2.25×10^{18} , and $1.19 \times 10^{19} \text{ cm}^{-3}$ respectively, highlighting the high crystalline quality of the

films. Figure 3(b) shows the rocking curves for the heteroepitaxial ($\bar{2}01$) β -Ga₂O₃ films, with smaller FWHMs of 293.04, 292.68, and 297.72 arc-sec for doping concentrations ranging from 1.15×10^{17} to 8.29×10^{18} cm⁻³, demonstrating superior crystalline quality compared to previously reported LPCVD, MBE, MOCVD-grown heteroepitaxial thin films [36, 37, 51-53].

In addition, both homo- and hetero-epitaxial β -Ga₂O₃ thin films were characterized using Raman spectroscopy to investigate their phonon modes and crystalline quality. The primitive unit cell of β -Ga₂O₃ consists of 10 atoms, resulting in 30 phonon modes, 27 of which are optical [54]. At the Γ -point, these modes belong to the irreducible representation $\Gamma^{\text{opt}} = 10A_g + 5B_g + 4A_u + 8B_u$, where the A_g and B_g modes are Raman active, and the A_u and B_u modes are infrared active. For excitation on the (010) plane, only A_g modes are observed in Raman spectra, as B_g modes are forbidden due to the symmetry of the crystal structure. The Raman spectra of the homoepitaxial (010) β -Ga₂O₃ films as shown in Figure 4(a) exhibits all A_g phonon modes, confirming the (010) orientation of the crystal. The peaks corresponding to A_g modes appear at 109.81, 169.8, 199.18, 319.67, 346.49, 415.84, 474.1, 629.31, 658.64, and 766.50 cm⁻¹, which align well with previously reported experimental and theoretical studies on β -Ga₂O₃ [36,38,54]. These modes represent a range of vibrational behaviors, including low-frequency modes (109.81, 169.8, and 199.18 cm⁻¹) related to the vibration and translation of tetrahedra-octahedra chains, mid-frequency modes (319.67, 346.49, 415.84, and 474.1 cm⁻¹) linked to Ga₂O₆ octahedra deformations, and high-frequency modes (629.31, 658.64, and 766.50 cm⁻¹) representing the bending and stretching of GaO₄ tetrahedra [38, 55-60]. Similarly, the Raman spectra of heteroepitaxial ($\bar{2}01$) β -Ga₂O₃ films grown on c-plane sapphire substrates are shown in Figure 4(b). Peaks at 114.14, 144.26, 474.1, and 652.45 cm⁻¹ correspond to B_g vibrational modes characteristic of the ($\bar{2}01$) orientation, while additional peaks at 169.27, 200.08, 319.32, 347.1, 416.2, 630.5, and 766.7 cm⁻¹ correspond to A_g

vibrational modes. The Raman spectra, exhibiting high-intensity and well-defined A_g and B_g modes, confirm the high crystalline quality and phase purity of both homo- and hetero-epitaxial β - Ga_2O_3 thin films, with no evidence of other Ga_2O_3 phases.

The transport characteristics of β - Ga_2O_3 films are also investigated using Hall measurement. By systematically adjusting the $SiCl_4$ flow, the carrier concentrations were effectively tuned. Figure 5 shows the RT mobility vs. carrier concentration for the films grown on both (010) β - Ga_2O_3 and off-axis c-sapphire with 6° miscut substrates. A clear correlation between doping concentration and Hall mobility was observed, with higher mobility at lower carrier concentrations. In pure β - Ga_2O_3 materials, the room-temperature mobility is typically limited by polar phonon scattering due to strong ionic Ga-O bonding. However, as doping increases, ionized impurity scattering, and neutral impurity scattering become dominant factors limiting the mobility. A similar trend was observed for ($\bar{2}01$) β - Ga_2O_3 films grown on sapphire substrates, where doping concentrations between 1.15×10^{17} and $8.29 \times 10^{18} \text{ cm}^{-3}$ were achieved. Table 1 provides a comprehensive summary of the films, detailing their thickness, growth rates, electron mobilities, and carrier concentrations. Both homoepitaxial and heteroepitaxial films exhibited high electron mobilities, with the maximum mobility of $162 \text{ cm}^2/Vs$ recorded for homoepitaxial films at a doping concentration of $1.51 \times 10^{17} \text{ cm}^{-3}$ - representing the highest reported mobility for LPCVD-grown homoepitaxial films. Similarly, heteroepitaxial β - Ga_2O_3 films grown on c-plane sapphire with a 6° offcut exhibited a record-high mobility of $149 \text{ cm}^2/Vs$ at a doping concentration of $1.15 \times 10^{17} \text{ cm}^{-3}$. Figure 5 also compares the RT mobility vs. carrier concentration of the films from this work to those grown by other techniques such as MOCVD [22-27,61-67], LPCVD [35-37], HVPE [20, 21], PLD [68], and MBE [41-46]. The results from this study demonstrate the promising mobilities achieved using the LPCVD system, with much faster growth rates (4.7-17 $\mu\text{m/hr}$) and thicker films

(2.3-11.7 μm), highlighting the potential of LPCVD growth system for producing high-quality thick $\beta\text{-Ga}_2\text{O}_3$ films with higher growth rates.

To better understand the charge carrier transport properties of LPCVD grown $\beta\text{-Ga}_2\text{O}_3$ films, temperature-dependent Hall measurements were also conducted on both homoepitaxial and heteroepitaxial thin films. Figures 6(a) and (b) display the temperature dependence of Hall mobility and carrier concentration for (010) $\beta\text{-Ga}_2\text{O}_3$ and ($\bar{2}01$) $\beta\text{-Ga}_2\text{O}_3$ films. The (010) $\beta\text{-Ga}_2\text{O}_3$ homoepitaxial films exhibited RT carrier concentrations of $5.05 \times 10^{17} \text{ cm}^{-3}$ and $8.29 \times 10^{17} \text{ cm}^{-3}$ with corresponding RT mobilities of 118 and $106 \text{ cm}^2/\text{V}\cdot\text{s}$, while the ($\bar{2}01$) $\beta\text{-Ga}_2\text{O}_3$ films showed RT carrier concentrations of $1.15 \times 10^{17} \text{ cm}^{-3}$ and $2.25 \times 10^{17} \text{ cm}^{-3}$, with corresponding mobilities of 149 and $124 \text{ cm}^2/\text{V}\cdot\text{s}$, respectively. For the two (010) $\beta\text{-Ga}_2\text{O}_3$ films, low temperature peak mobilities of $332 \text{ cm}^2/\text{V}\cdot\text{s}$ and $219 \text{ cm}^2/\text{V}\cdot\text{s}$ was achieved at 96K and 112K temperatures, respectively with carrier concentrations of $1.55 \times 10^{17} \text{ cm}^{-3}$ and $3.86 \times 10^{17} \text{ cm}^{-3}$ as shown in Figure 6(a). Similarly, a record-high low-temperature peak mobilities from the ($\bar{2}01$) $\beta\text{-Ga}_2\text{O}_3$ films exceeding $843 \text{ cm}^2/\text{V}\cdot\text{s}$ and $498 \text{ cm}^2/\text{V}\cdot\text{s}$ were observed at 80 K temperature with carrier concentrations of $1.74 \times 10^{16} \text{ cm}^{-3}$ and $3.24 \times 10^{16} \text{ cm}^{-3}$, respectively, indicating the high purity and low compensating defect levels in the ($\bar{2}01$) $\beta\text{-Ga}_2\text{O}_3$ films. All these films exhibited mobility enhancement as the temperature decreases. Notably, electron mobility in $\beta\text{-Ga}_2\text{O}_3$ is primarily limited by ionized impurity scattering at low temperatures and optical phonon scattering at higher temperatures. The donor activation energy (E_D) with donor (N_D) and compensation (N_A) concentrations were extracted by fitting the temperature dependent transport data using the charge neutrality equation ($n + N_A = \frac{N_D}{1 + 2e^{-\frac{-(E_D - E_F)}{k_B T}}}$), where N_A is the concentration of acceptors acting as compensators, N_D is the donor concentration, and E_D is the donor activation energy. The

extracted activation energies of 13.2 and 7 meV are calculated for the two (010) β -Ga₂O₃ homoepitaxial films with donor concentrations of $8.2 \times 10^{17} \text{ cm}^{-3}$ and $1.5 \times 10^{18} \text{ cm}^{-3}$, respectively with corresponding N_A of $\sim 3 \times 10^{15} \text{ cm}^{-3}$ and $\sim 5 \times 10^{15} \text{ cm}^{-3}$. A similar donor activation energy of β -Ga₂O₃ has been previously reported at comparable doping levels [69]. The donor activation energies reduce as the donor concentration increase, which is consistent with the findings from β -Ga₂O₃ films investigated with different carrier concentrations [69]. Such decrease in donor activation energies is expected for highly doped semiconductors when an impurity band begins to form [70,71]. Similar trend of a reduction of donor activation energy with the increase in Si doping concentration was also observed in highly Si-doped ($5.2 \times 10^{18} \text{ cm}^{-3} < N_d < 1.5 \times 10^{19} \text{ cm}^{-3}$) AlGaIn films [72]. as well as Si doped β -(Al_xGa_{1-x})₂O₃ films [73]. In case of ($\bar{2}01$) β -Ga₂O₃ films, donor concentrations of $1.39 \times 10^{17} \text{ cm}^{-3}$ and $3.1 \times 10^{17} \text{ cm}^{-3}$ with corresponding N_A of $\sim 2 \times 10^{15} \text{ cm}^{-3}$ and $\sim 5 \times 10^{15} \text{ cm}^{-3}$ were extracted with donor activation energies of 24 and 22 meV, respectively, aligning with previously reported values [36].

To further correlate the SiCl₄ flow rates with doping concentration, the C-V measurements were conducted on $\sim 6.8 \mu\text{m}$ thick homoepitaxial β -Ga₂O₃ films grown on Sn doped (010) β -Ga₂O₃ substrates, as shown in Figure 7. A schematic cross section of the Schottky diode structure used for this measurement is shown in the inset of Figure 7(a). A monotonous increase in capacitance is observed with the increase in SiCl₄ flow rates. The net charge density ($N_D^+ - N_A^-$) values of $8.49 \times 10^{17} \text{ cm}^{-3}$, $1.11 \times 10^{18} \text{ cm}^{-3}$ and $2.44 \times 10^{18} \text{ cm}^{-3}$ are extracted from the C-V charge profile and are plotted in Figure 7(b) for SiCl₄ flow rates of 0.07, 08 and 0.10 SCCM, respectively. These results indicate that increasing SiCl₄ flow rates leads to higher carrier concentrations, with the $N_D^+ - N_A^-$ values remaining nearly uniform across the depth profile.

To evaluate impurity concentrations, SIMS characterization was conducted on a representative homoepitaxial (010) β -Ga₂O₃ film with the highest recorded mobility of 162 cm²/Vs, as shown in Figure 8. The analysis revealed a uniform Si distribution throughout the 3.4 μ m-thick epilayer, with an average concentration of approximately $\sim 4.5 \times 10^{17}$ cm⁻³, exceeding the carrier concentration of 1.51×10^{17} cm⁻³ measured by Hall, indicating low activation ratio of Si dopants in the sample. These corroborates well with recent findings from deep level defects investigation in LPCVD grown (010) β -Ga₂O₃ [39] and can be attributed to the compensation effects caused by native defects unique to the LPCVD growth process. That study using deep-level optical spectroscopy (DLOS) on LPCVD-grown β -Ga₂O₃ have revealed a dominant defect at $E_C - 3.6$ eV [39]. This defect, which has not been reported in β -Ga₂O₃ grown by other methods such as MOCVD and MBE, is a prominent feature in the LPCVD defect spectrum and is believed to act as a strong acceptor-like trap center within the bandgap with concentrations in the mid- 10^{15} cm⁻³ range [39]. Further support for this observation comes from DFT calculations, which predict that oxygen vacancies ($V_{O(III)}^+$) or hydrogenated gallium vacancies ($V_{Ga} - nH$) could create energy levels near $E_C - 3.6$ eV [74,75]. Although the Si donor ionization energy of < 40 meV in β -Ga₂O₃ suggests full ionization at room temperature [39,69], the presence of these defects likely trap free carriers, effectively compensating the Si donors and reducing the net carrier concentration. A distinct Si peak was observed at the epilayer/substrate interface in Figure 8, a common feature likely due to surface contamination or residue from substrate processing, as noted in previous studies by LPCVD [35,37], MOCVD [22,23], HVPE [76] and MBE [43,44]. Additionally, carbon and hydrogen concentrations in the films were also investigated by quantitative SIMS, since they can originate from the growth environment, precursors, or instrument components. However, the SIMS results revealed that both carbon and hydrogen levels are below their detection limits. SIMS

analysis also confirmed that the Cl concentration is also below the detection limit, indicating the suitability of using SiCl₄ as a n-type doping precursor in LPCVD system for achieving high-purity films with controllable low doping.

In summary, LPCVD growth of Si doped β -Ga₂O₃ films with promising electron transport characteristics have been demonstrated on both (010) Ga₂O₃ and off-axis c-sapphire substrates. The surface morphology of the films showed a strong dependence on carrier concentrations, with lower doping resulting in smoother surfaces and higher electron mobility. Surface AFM analysis revealed RMS roughness values as low as 2.65 nm for homoepitaxial films, and ranging between 4.29-5.14 nm for heteroepitaxial β -Ga₂O₃ films. High resolution XRD and Raman measurement confirmed the high crystalline quality and phase purity of the films, with distinct A_g and B_g phonon modes in Raman spectra and no additional phases detected in XRD. Hall measurements showed promising electron mobilities, with a highest RT mobility of 162 cm²/Vs for homoepitaxial films and 149 cm²/Vs for heteroepitaxial films at corresponding RT carrier concentrations of 1.51×10^{17} cm⁻³ and 1.15×10^{17} cm⁻³ respectively, while temperature-dependent measurements revealed peak mobilities exceeding 843 cm²/Vs at low temperatures (80 K) for the heteroepitaxial film. Donor activation energies ranged from 7 to 24 meV, increasing as doping concentrations decreased. SIMS analysis further confirmed uniform Si distribution and ultra-low impurity concentrations, highlighting high-purity of LPCVD grown β -Ga₂O₃ films. These results highlight the potential of LPCVD growth system for producing high-quality, thick β -Ga₂O₃ films with promising transport properties.

Data Availability

The data that support the findings of this study are available from the corresponding author upon reasonable request.

References

- [1] A.J. Green, J. Speck, G. Xing, P. Moens, F. Allerstam, K. Gumaelius, T. Neyer, A. Arias-Purdue, V. Mehrotra, A. Kuramata, K. Sasaki, S. Watanabe, K. Koshi, J. Blevins, O. Bierwagen, S. Krishnamoorthy, K. Leedy, A.R. Arehart, A.T. Neal, S. Mou, S.A. Ringel, A. Kumar, A. Sharma, K. Ghosh, U. Singiseti, W. Li, K. Chabak, K. Liddy, A. Islam, S. Rajan, S. Graham, S. Choi, Z. Cheng, and M. Higashiwaki, *APL Materials* **10**, 029201 (2022).
- [2] A. Kuramata, K. Koshi, S. Watanabe, Y. Yamaoka, T. Masui, and S. Yamakoshi, *Jpn. J. Appl. Phys.* **55**, 1202A2 (2016).
- [3] K. Konishi, K. Goto, H. Murakami, Y. Kumagai, A. Kuramata, S. Yamakoshi, and M. Higashiwaki, *Appl. Phys. Lett.* **110**, 103506 (2017).
- [4] W. Li, K. Nomoto, Z. Hu, D. Jena, and H. G. Xing, *IEEE Electron Device Lett.* **41**, 107 (2020).
- [5] W. Li, Z. Hu, K. Nomoto, Z. Zhang, J.-Y. Hsu, Q. T. Thieu, K. Sasaki, A. Kuramata, D. Jena, and H. G. Xing, *Appl. Phys. Lett.* **113**, 202101 (2018).
- [6] W. Li, Z. Hu, K. Nomoto, R. Jinno, Z. Zhang, Q. T. Thieu, K. Sasaki, A. Kuramata, D. Jena, and H. G. Xing, *IEEE IEDM Technical Digest* (2018), p. 8.5.1.
- [7] S. Roy, A. Bhattacharyya, P. Ranga, H. Splawn, J. Leach, and S. Krishnamoorthy, *IEEE Electron Device Lett.* **42**, 1140 (2021).
- [8] Z. Jian, S. Mohanty, and E. Ahmadi, *Appl. Phys. Lett.* **116**, 152104 (2020).
- [9] J. Yang, S. Ahn, F. Ren, S. J. Pearton, S. Jang, and A. Kuramata, *IEEE Electron Device Lett.* **38**, 906 (2017).
- [10] C. Joishi, S. Rafique, Z. Xia, L. Han, S. Krishnamoorthy, Y. Zhang, S. Lodha, H. Zhao, and S. Rajan, *Appl. Phys. Express* **11**, 031101 (2018).
- [11] C.-H. Lin, Y. Yuda, M. H. Wong, M. Sato, N. Takekawa, K. Konishi, T. Watahiki, M. Yamamuka, H. Murakami, Y. Kumagai, and M. Higashiwaki, *IEEE Electron Device Lett.* **40**, 1487 (2019).
- [12] S. Kumar, H. Murakami, Y. Kumagai, and M. Higashiwaki, *Appl. Phys. Express* **15**, 054001 (2022).
- [13] S. A. Khan, S. Saha, U Singiseti, A. Bhuiyan, Radiation Resilience of β -Ga₂O₃ Schottky Barrier Diodes Under High Dose Gamma Radiation, *Journal of Applied Physics*, (accepted for publication) (2024).
- [14] E. Farzana, A. Bhattacharyya, N. S. Hendricks, T. Itoh, S. Krishnamoorthy, and J. S. Speck, *APL Mater.* **10**, 111104 (2022).
- [15] A. Gilankar, A. Katta, N. Das, N. K. Kalarickal, arXiv:2409.00344 (2024).
- [16] S. Saha, L. Meng, D.S. Yu, A. Bhuiyan, H. Zhao, and U. Singiseti, *Journal of Vacuum Science & Technology A* **42**, 042705 (2024).
- [17] S. Saha, L. Meng, Z. Feng, A. Bhuiyan, H. Zhao, and U. Singiseti, *Applied Physics Letters* **120**, 122106 (2022).
- [18] S. Saha, L. Meng, A. Bhuiyan, A. Sharma, C.N. Saha, H. Zhao, and U. Singiseti, *Applied Physics Letters* **123**, 132105 (2023).
- [19] H. Murakami, K. Nomura, K. Goto, K. Sasaki, K. Kawara, Q.T. Thieu, R. Togashi, Y. Kumagai, M. Higashiwaki, A. Kuramata, S. Yamakoshi, B. Monemar, and A. Koukitu, *Applied Physics Express* **8**, 015503 (2014).

- [20] K. Goto, K. Konishi, H. Murakami, Y. Kumagai, B. Monemar, M. Higashiwaki, A. Kuramata, and S. Yamakoshi, *Thin Solid Films* **666**, 182-184 (2018).
- [21] J.H. Leach, K. Uduary, J. Rumsey, G. Dodson, H. Splawn, and K.R. Evans, *APL Materials* **7**, 022504 (2018).
- [22] Z. Feng, A Bhuiyan, Z. Xia, W. Moore, Z. Chen, J.F. McGlone, D.R. Daughton, A.R. Arehart, S.A. Ringel, S. Rajan, and H. Zhao, *Physica Status Solidi (RRL) – Rapid Research Letters* **14**, 2000145 (2020).
- [23] Z. Feng, A.F.M Anhar Uddin Bhuiyan, M.R. Karim, and H. Zhao, *Applied Physics Letters* **114**, 250601 (2019).
- [24] L. Meng, Z. Feng, A.F. Bhuiyan, and H. Zhao, *Crystal Growth & Design* **22**, 3896-3904 (2022).
- [25] F. Alema, Y. Zhang, A. Osinsky, N. Orishchin, N. Valente, A. Mauze, and J.S. Speck, *APL Materials* **8**, 021110 (2020).
- [26] S. Bin Anooz, R. Grüneberg, C. Wouters, R. Schewski, M. Albrecht, A. Fiedler, K. Irmscher, Z. Galazka, W. Miller, G. Wagner, J. Schwarzkopf, and A. Popp, *Applied Physics Letters* **116**, Q3040-Q3044 (2020).
- [27] Y. Zhang, F. Alema, A. Mauze, O.S. Koksaldi, R. Miller, A. Osinsky, and J.S. Speck, *APL Materials* **7**, 022506 (2018).
- [28] A. Bhattacharyya, C. Peterson, K. Chanchaiworawit, S. Roy, Y. Liu, S. Rebollo, and S. Krishnamoorthy, *Applied Physics Letters* **124**, 010601 (2024).
- [29] L. Meng, A.F. Bhuiyan, D.S. Yu, H.L. Huang, J. Hwang, and H. Zhao, *Crystal Growth & Design* **23**, 7365 (2023).
- [30] A.F. Bhuiyan, Z. Feng, L. Meng, and H. Zhao, *Journal of Applied Physics* **133**, 211103 (2023).
- [31] L. Meng, A.F. Bhuiyan, and H. Zhao, *Applied Physics Letters* **122**, 232106 (2023).
- [32] Bhuiyan, A. F. M. A. U. (2023). Metalorganic chemical vapor deposition of ultrawide bandgap $(\text{Al}_x\text{Ga}_{1-x})_2\text{O}_3$ for next generation power electronics [Doctoral dissertation, Ohio State University]. OhioLINK Electronic Theses and Dissertations Center. http://rave.ohiolink.edu/etdc/view?acc_num=osu1689886516141118
- [33] Z. Feng, A.F. Bhuiyan, N.K. Kalarickal, S. Rajan, and H. Zhao, *Applied Physics Letters* **117**, 222106 (2020).
- [34] Z. Feng, M.R. Karim, and H. Zhao, *APL Materials* **7**, 022514 (2018).
- [35] Y. Zhang, Z. Feng, M.R. Karim, and H. Zhao, *Journal of Vacuum Science & Technology A: Vacuum, Surfaces, and Films* **38**, 050806 (2020).
- [36] S. Rafique, L. Han, A.T. Neal, S. Mou, J. Boeckl, and H. Zhao, *Physica Status Solidi (a)* **215**, 1700467 (2017).
- [37] S. Rafique, M.R. Karim, J.M. Johnson, J. Hwang, and H. Zhao, *Applied Physics Letters* **112**, 052104 (2018).
- [38] S. Rafique, L. Han, M.J. Tadjer, J.A. Freitas, N.A. Mahadik, and H. Zhao, *Applied Physics Letters* **108**, 182105 (2016)
- [39] H. Ghadi, J.F. McGlone, E. Cornuelle, Z. Feng, Y. Zhang, L. Meng, H. Zhao, A.R. Arehart, and S.A. Ringel, *APL Materials* **10**, 101110 (2022).
- [40] S. Saha, L. Meng, Z. Feng, A.F. Anhar Uddin Bhuiyan, H. Zhao, and U. Singiseti, *Applied Physics Letters* **120**, 122106 (2022).
- [41] K. Sasaki, A. Kuramata, T. Masui, E.G. Villora, K. Shimamura, and S. Yamakoshi, *Applied Physics Express* **5**, 035502 (2012).

- [42] A. Mauze, Y. Zhang, T. Itoh, E. Ahmadi, and J.S. Speck, *Applied Physics Letters* **117**, 222102 (2020).
- [43] E. Ahmadi, O.S. Koksaldi, S.W. Kaun, Y. Oshima, D.B. Short, U.K. Mishra, and J.S. Speck, *Applied Physics Express* **10**, 041102 (2017).
- [44] J.P. McCandless, V. Protasenko, B.W. Morell, E. Steinbrunner, A.T. Neal, N. Tanen, Y. Cho, T.J. Asel, S. Mou, P. Vogt, H.G. Xing, and D. Jena, *Applied Physics Letters* **121**, 072108 (2022).
- [45] K. Azizie, F.V. Hensling, C.A. Gorsak, Y. Kim, N.A. Pieczulewski, D.M. Dryden, M.K. Senevirathna, S. Coye, S.-L. Shang, J. Steele, P. Vogt, N.A. Parker, Y.A. Birkhölzer, J.P. McCandless, D. Jena, H.G. Xing, Z.-K. Liu, M.D. Williams, A.J. Green, K. Chabak, D.A. Muller, A.T. Neal, S. Mou, M.O. Thompson, H.P. Nair, and D.G. Schlom, *APL Materials* **11**, 041102 (2023).
- [46] Z. Wen, K. Khan, X. Zhai, and E. Ahmadi, *Applied Physics Letters* **122**, 082101 (2023).
- [47] Z. Wen, X. Zhai, C. Lee, S. Kosanovic, Y. Kim, A.T. Neal, T. Asel, S. Mou, and E. Ahmadi, *Applied Physics Letters* **124**, 122101 (2024).
- [48] Z. Wen, X. Zhai, K. Khan, O. Odabasi, M. Kim, and E. Ahmadi, *Applied Physics Letters* **125**, 162103 (2024).
- [49] M.A. Filho, W. Farmer, C.-L. Hsiao, R.B. dos Santos, L. Hultman, J. Birch, K. Ankit, and G.K. Gueorguiev, *Crystal Growth & Design* **24**, 4717 (2024).
- [50] M. Alves Machado Filho, C.-L. Hsiao, R.B. dos Santos, L. Hultman, J. Birch, and G.K. Gueorguiev, *ACS Nanoscience Au* **3**, 84 (2022).
- [51] X. Z. Liu, P. Guo, T. Sheng, L. X. Qian, W. L. Zhang, Y. R. Li, *Opt. Mater.* **51**, 203 (2016).
- [52] Y. Chen, H. Liang, X. Xia, P. Tao, R. Shen, Y. Liu, Y. Feng, Y. Zheng, X. Li, G. Du, *J. Mater. Sci. Mater. Electron.* **26**, 3231 (2015).
- [53] M. J. Tadjer, M. A. Mastro, N. A. Mahadik, M. Currie, V. D. Wheeler, J. A. Freitas Jr., J. D. Greenlee, J. K. Hite, K. D. Hobart, C. R. Eddy, Jr., F. J. Kub, *J. Electron. Mater.* **45**, 2031-2037 (2016).
- [54] C. Kranert, C. Sturm, R. Schmidt-Grund, and M. Grundmann, *Scientific Reports* **6**, 35964 (2016).
- [55] D. Dohy, G. Lucazeau, and A. Revcolevschi, *Journal of Solid State Chemistry* **45**, 180 (1982).
- [56] X.-Q. Shen, M. Shimizu, and H. Okumura, *Japanese Journal of Applied Physics* **42**, L1293 (2003).
- [57] X. Du, W. Mi, C. Luan, Z. Li, C. Xia, and J. Ma, *Journal of Crystal Growth* **404**, 75 (2014).
- [58] X. Du, Z. Li, C. Luan, W. Wang, M. Wang, X. Feng, H. Xiao, and J. Ma, *Journal of Materials Science* **50**, 3252 (2015).
- [59] D. Gogova, M. Schmidbauer, and A. Kwasniewski, *CrystEngComm* **17**, 6744 (2015).
- [60] S. Kumar, G. Sarau, C. Tessarek, M.Y. Bashouti, A. Hähnel, S. Christiansen, and R. Singh, *Journal of Physics D: Applied Physics* **47**, 435101 (2014).
- [61] A. Bhattacharyya, P. Ranga, S. Roy, J. Ogle, L. Whittaker-Brooks, and S. Krishnamoorthy, *Applied Physics Letters* **117**, 142102 (2020).
- [62] M. Baldini, M. Albrecht, A. Fiedler, K. Irmscher, R. Schewski, and G. Wagner, *ECS Journal of Solid State Science and Technology* **6**, Q3040-Q3044 (2016).
- [63] T.-S. Chou, P. Seyidov, S. Bin Anooz, R. Grüneberg, T.T. Tran, K. Irmscher, M. Albrecht, Z. Galazka, J. Schwarzkopf, and A. Popp, *AIP Advances* **11**, 115323 (2021).

- [64] F. Alema, Y. Zhang, A. Mauze, T. Itoh, J.S. Speck, B. Hertog, and A. Osinsky, *AIP Advances* **10**, 085002 (2020).
- [65] C. Peterson, A. Bhattacharyya, K. Chanchaiworawit, R. Kahler, S. Roy, Y. Liu, S. Rebollo, A. Kallistova, T.E. Mates, and S. Krishnamoorthy, *Applied Physics Letters* **125**, 182103 (2024).
- [66] G. Seryogin, F. Alema, N. Valente, H. Fu, E. Steinbrunner, A.T. Neal, S. Mou, A. Fine, and A. Osinsky, *Applied Physics Letters* **117**, 262101 (2020).
- [67] F. Alema, G. Seryogin, A. Osinsky, and A. Osinsky, *APL Materials* **9**, 091102 (2021).
- [68] K.D. Leedy, K.D. Chabak, V. Vasilyev, D.C. Look, K. Mahalingam, J.L. Brown, A.J. Green, C.T. Bowers, A. Crespo, D.B. Thomson, and G.H. Jessen, *APL Materials* **6**, 101102 (2018).
- [69] A.T. Neal, S. Mou, S. Rafique, H. Zhao, E. Ahmadi, J.S. Speck, K.T. Stevens, J.D. Blevins, D.B. Thomson, N. Moser, K.D. Chabak, and G.H. Jessen, *Applied Physics Letters* **113**, (2018).
- [70] E. M. Conwell, *Phys. Rev.* **103**, 51 (1956).
- [71] N. F. Mott, *Rev. Mod. Phys.* **40**, 677 (1968).
- [72] S. Bharadwaj, S. M. Islam, K. Nomoto, V. Protasenko, A. Chaney, H. G. Xing, and D. Jena, *Appl. Phys. Lett.* **114**, 113501 (2019).
- [73] A. Bhuiyan, Z. Feng, L. Meng, A. Fiedler, H.-L. Huang, A.T. Neal, E. Steinbrunner, S. Mou, J. Hwang, S. Rajan, and H. Zhao, *Journal of Applied Physics* **131**, 145301 (2022).
- [74] J.B. Varley, J.R. Weber, A. Janotti, and C.G. Van de Walle, *Applied Physics Letters* **97**, 142106 (2010).
- [75] J.B. Varley, H. Peelaers, A. Janotti, and C.G. Van de Walle, *Journal of Physics: Condensed Matter* **23**, 334212 (2011).
- [76] H. Murakami, K. Nomura, K. Goto, K. Sasaki, K. Kawara, Q.T. Thieu, R. Togashi, Y. Kumagai, M. Higashiwaki, A. Kuramata, S. Yamakoshi, B. Monemar, and A. Koukitu, *Applied Physics Express* **8**, 015503 (2014).

Table 1

Summary of film thickness, growth rates and transport characteristics of homo- and hetero-epitaxial β -Ga₂O₃ films.

Substrate	Estimated Thickness (μm)	Growth Rate ($\mu\text{m/hr}$)	Hall Mobility (cm^2/Vs)	Carrier Concentration (cm^{-3})
Fe doped (010) β -Ga ₂ O ₃	3.87	7.74	118	5.05×10^{17}
	3.40	6.80	162	1.51×10^{17}
	3.89	7.78	92	1.41×10^{18}
	3.37	6.74	101	2.25×10^{18}
	4.78	9.56	106	8.29×10^{17}
	3.77	7.54	81	1.19×10^{19}
	2.34	4.68	113	1.25×10^{18}
C-plane sapphire with 6° offcut	11.10	11.10	138	2.99×10^{17}
	10.15	10.15	149	1.15×10^{17}
	9.20	9.20	124	2.22×10^{17}
	6.09	12.18	118	3.26×10^{17}
	11.70	11.70	109	3.68×10^{17}
	11.47	11.47	81	1.46×10^{18}
	8.49	16.98	94	5.59×10^{17}
	5.16	10.32	74	1.70×10^{18}
10.31	10.31	59	8.29×10^{18}	

Figure Captions

Figure 1. Surface view of FESEM images of β -Ga₂O₃ films grown on (a-c) (010) β -Ga₂O₃ and (d-f) 6° off-axis c-plane sapphire substrates with different carrier concentrations.

Figure 2. AFM surface images of β -Ga₂O₃ films grown on (a-b) (010) β -Ga₂O₃ and (c-d) 6° off-axis c-plane sapphire substrates, indicating their corresponding surface RMS roughness.

Figure 3. XRD rocking curves for β -Ga₂O₃ films: (a) homoepitaxially grown films on (010) β -Ga₂O₃ substrate, inset shows a wide ω -2 θ scan indicating (020) β -Ga₂O₃ peak (b) hetero-epitaxially grown films on c-plane sapphire with inset showing ($\bar{4}02$) and ($\bar{8}04$) peaks of ($\bar{2}01$) oriented β -Ga₂O₃ films from ω -2 θ scan.

Figure 4. Room temperature Raman spectra of (a) homo- and (b) hetero-epitaxial β -Ga₂O₃ films.

Figure 5. Benchmarking plot of the measured transport properties of β -Ga₂O₃ films (RT Hall mobility vs carrier concentration) obtained in this work with values reported in the literature for various growth techniques, including LPCVD [35-37], MOCVD [22-27,61-67], HVPE [20,21], MBE [41-46] and PLD [68].

Figure 6. (a) Temperature dependent carrier mobility as a function of temperature for both homo- and hetero-epitaxial films grown with various doping concentrations. (b) Measured carrier concentration as a function of 1000/T and the calculated concentration from the charge neutrality equations. Colored circles represent experimental data points and dashed lines are obtained from the calculation.

Figure 7: (a) C-V characteristics of β -Ga₂O₃ Schottky barrier diodes fabricated using LPCVD grown β -Ga₂O₃ (010) drift layers with three different SiCl₄ flow rates. (b) Net carrier concentration profile for all three samples derived from the C-V curves, showing flat charge profile.

Figure 8: Quantitative SIMS impurity (Si, C, H and Cl) depth profile of (010) β -Ga₂O₃ homoepitaxial film.

Figure 1

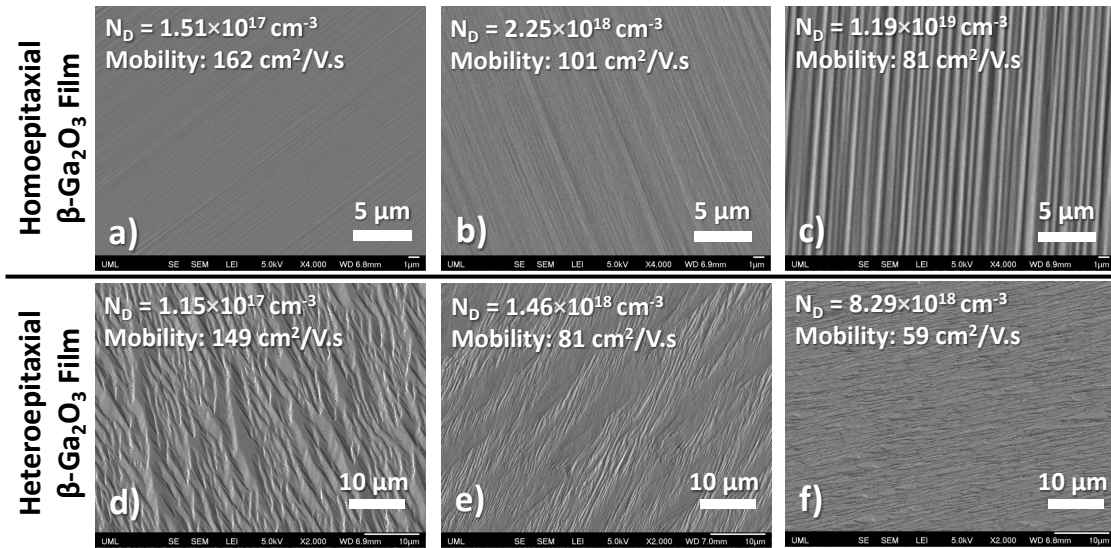


Figure 2

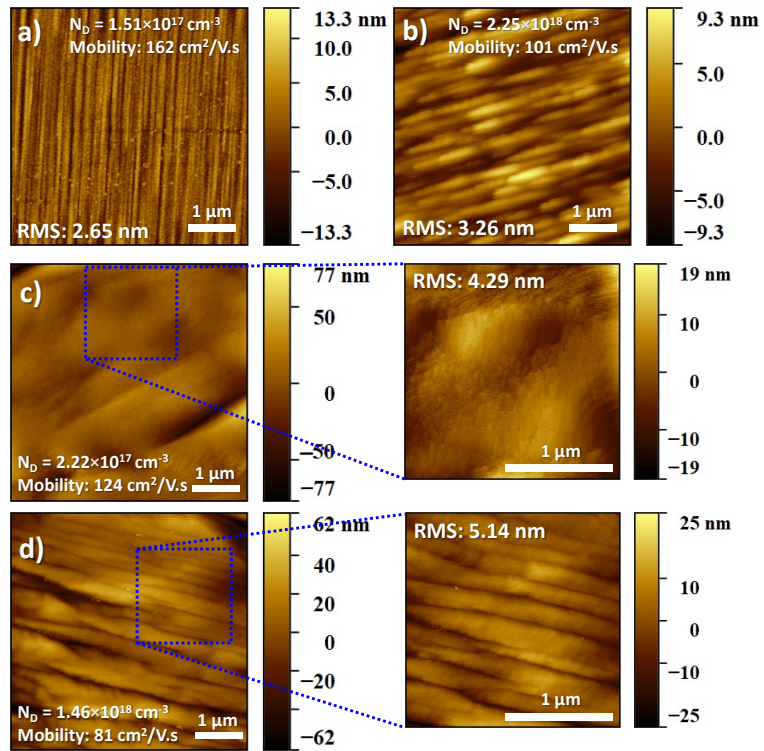


Figure 3

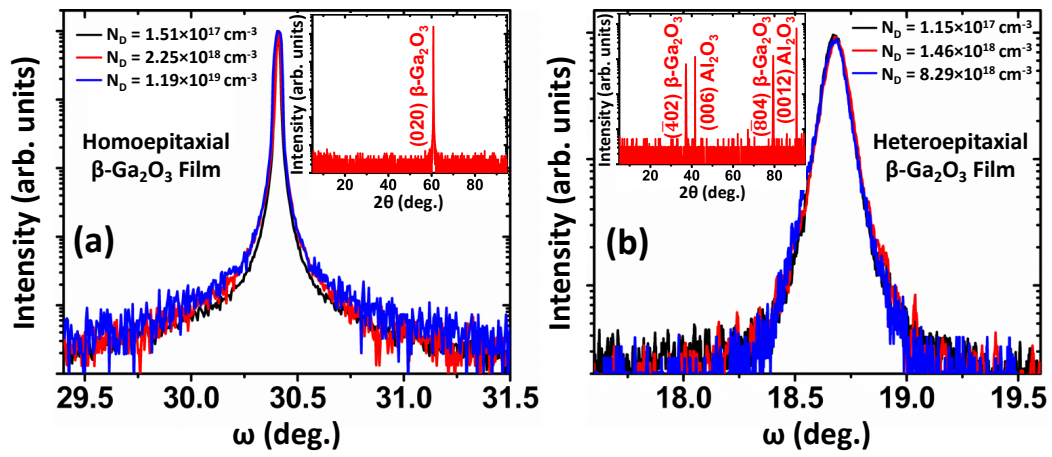


Figure 4

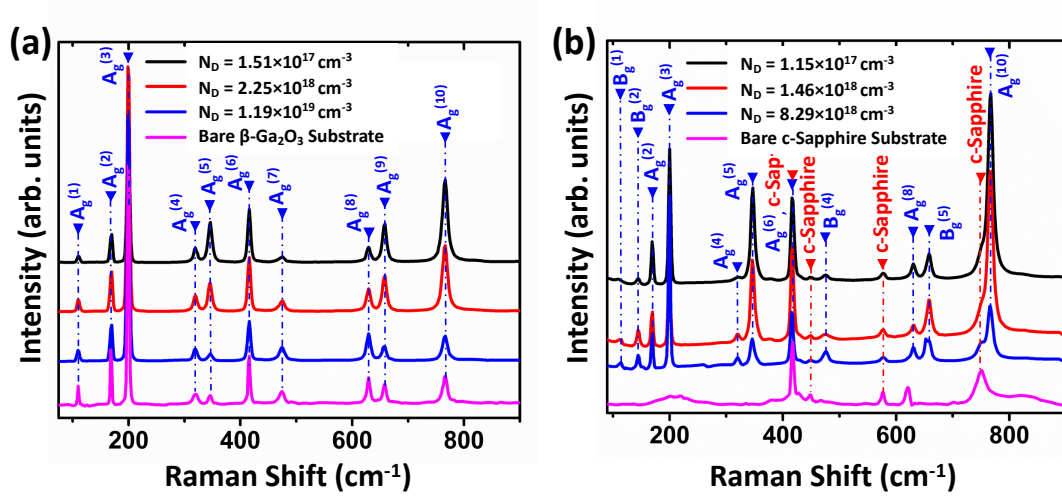


Figure 5

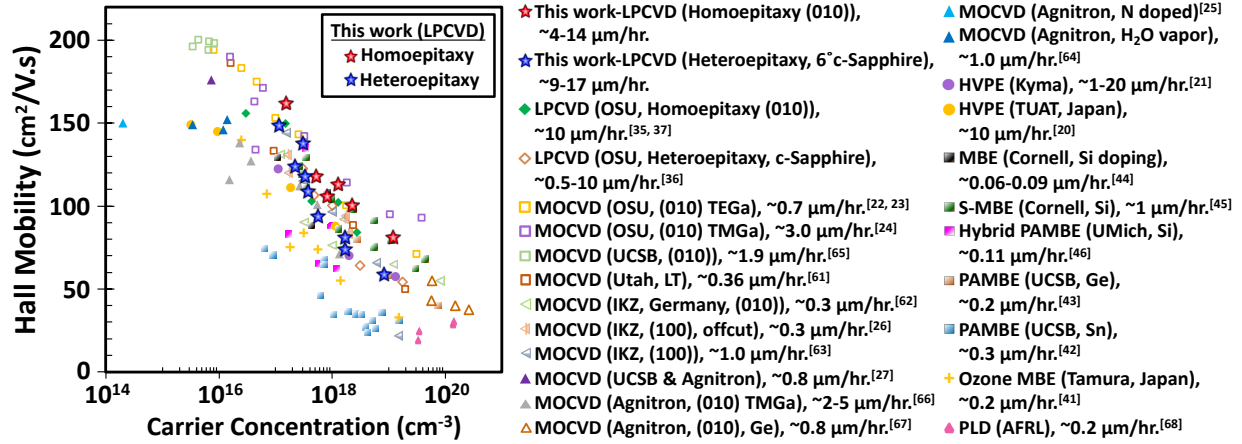


Figure 6

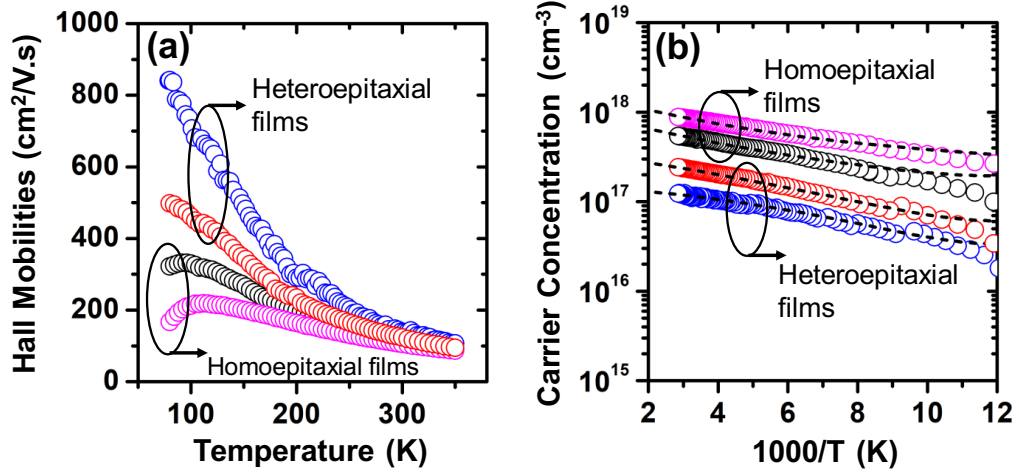


Figure 7

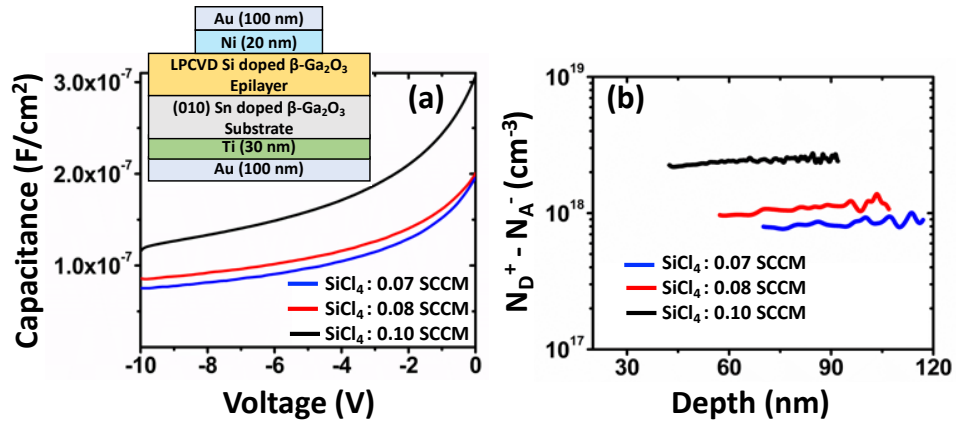


Figure 8

